



HAL
open science

Applications of the Oxford-JEOL Aberration Corrected Electron Microscope

Peter D Nellist, Angus Kirkland

► **To cite this version:**

Peter D Nellist, Angus Kirkland. Applications of the Oxford-JEOL Aberration Corrected Electron Microscope. *Philosophical Magazine*, 2010, 90 (35-36), pp.4751-4767. 10.1080/14786435.2010.516775 . hal-00633211

HAL Id: hal-00633211

<https://hal.science/hal-00633211>

Submitted on 18 Oct 2011

HAL is a multi-disciplinary open access archive for the deposit and dissemination of scientific research documents, whether they are published or not. The documents may come from teaching and research institutions in France or abroad, or from public or private research centers.

L'archive ouverte pluridisciplinaire **HAL**, est destinée au dépôt et à la diffusion de documents scientifiques de niveau recherche, publiés ou non, émanant des établissements d'enseignement et de recherche français ou étrangers, des laboratoires publics ou privés.



**Applications of the Oxford-JEOL Aberration Corrected
Electron Microscope**

Journal:	<i>Philosophical Magazine & Philosophical Magazine Letters</i>
Manuscript ID:	TPHM-10-Mar-0102.R1
Journal Selection:	Philosophical Magazine
Date Submitted by the Author:	12-Aug-2010
Complete List of Authors:	Nellist, Peter; University of Oxford, Department of Materials Kirkland, Angus; Oxford University
Keywords:	aberration correction, HRTEM, STEM
Keywords (user supplied):	confocal microscopy

SCHOLARONE™
Manuscripts

Applications of the Oxford-JEOL Aberration Corrected Electron Microscope

P.D.Nellist* and A.I.Kirkland*

**Department of Materials, University of Oxford, Parks Road, Oxford, OX1 3PH, UK*

In this contribution we review the use of aberration corrected electron microscopy at Oxford from 2003 to the present day. In particular, the following examples of work carried out in Oxford during this period are described: aberration-corrected exit wavefunction reconstruction is used to examine the surface structure of a catalyst nanoparticle; it is shown that tilt-series reconstruction can retrieve higher spatial resolution information; the Z-contrast nature of annular dark field scanning transmission electron microscopy is used to quantitatively locate dopant atoms in an intergranular film; the recording of annular dark field images on an absolute intensity scale is demonstrated; finally it is shown that confocal trajectories can dramatically improve the depth resolution for optical sectioning.

Keywords: aberration correction, HRTEM, STEM, confocal microscopy

1. Introduction

The appointment of David Cockayne as Professor in the Physical Examination of Materials in 2000 approximately coincided with the availability of commercial electron optical elements for correction of the inherent spherical aberration present in round electromagnetic objective lenses. Under Cockayne's leadership, the Electron Microscopy and Analysis group at Oxford was at the forefront of this revolution having been successful in obtaining funding for a unique instrument fitted, for the first time, with aberration correctors *both before* the sample for scanning transmission electron microscopy (STEM) *and after* the sample for conventional high resolution transmission electron microscopy (HRTEM). The ambitious instrumental development required was undertaken in collaboration with JEOL Ltd and the first instrument, the Oxford-JEOL 2200FS (OJ1), was installed in September 2003 and fully commissioned by the end of that year. This instrument operated successfully until late 2006 when it was replaced with an improved version (the JEOL 2200MCO (OJ2)) which remains in operation.

The detailed configuration, specification and operation of the OJ1 instrument (Figure 1 (a)) have been described previously [1, 2]. This instrument, which was subsequently commercialised by JEOL in a number of optical variants, was fitted with: a thermally-assisted Schottky field-emission gun; pre-specimen optics containing an aberration corrector, capable of illuminating the sample with either plane-wave illumination, for HRTEM, or providing a focused probe for STEM; a large area EDX detector; a post-sample aberration corrector for HRTEM; an in-column omega energy-filter [3]; STEM bright-field and dark-field detectors; a TV-

1
2
3 rate CCD camera; and a 2048 x 2048 pixel high-resolution CCD camera. The
4
5 replacement OJ2 instrument (Figure 1(b)) embodied a number of design modifications
6
7 including improvements to the stability of the high-tension source (using twin HT
8
9 tanks) and objective lens power supplies, a new mechanical frame, pre and post
10
11 specimen high-speed piezo shutters and additional intermediate and projector lenses
12
13 in addition to a larger 4096 x 4096 pixel CCD camera.
14
15
16
17
18
19

20 The purpose of this paper is to provide a review of the operation and
21
22 application of both instruments. Their performance in both HRTEM and STEM
23
24 modes will be illustrated with examples taken from research themes addressed by a
25
26 number of different researchers in the Oxford EM group. Research at Oxford into
27
28 novel methods that made use of the unique capabilities of these instruments will also
29
30 be reviewed.
31
32
33
34
35

36 **2. Aberration-Corrected High Resolution TEM Imaging and Exit Wavefunction** 37 **Reconstruction** 38

39
40 The aberration correctors fitted to both OJ1 and OJ2 instruments were supplied by
41
42 CEOS GmbH, based on a design originally due to Rose [4, 5]. In this arrangement,
43
44 two sextupole elements are used to generate negative spherical aberration, and are
45
46 coupled *via* a round-lens doublet such that one is conjugate to the other, but with a
47
48 180° rotation, produced by the transfer doublet such that the first-order effect of three-
49
50 fold astigmatism is cancelled. Crucially, the sextupoles are also coupled to the
51
52 objective lens by a further round-lens doublet so that off-axial aberrations are also
53
54 corrected in the aplanatic arrangement that is required for HRTEM imaging. Whilst
55
56 this configuration results in minimal 5th-order aberrations, the need for the sextupole
57
58 elements to be optically conjugate to the objective lens precludes direct, independent
59
60

1
2
3 control of the 5th-order aberrations under aplanatic conditions [6]. In the OJ2
4 instrument these residual aberrations have been measured to be approximately 2 mm
5
6
7
8 for both the round fifth order aberration (C_5) and six-fold astigmatism (A_5).
9

10
11
12 Phase contrast imaging in the TEM depends critically on the lens aberrations
13 that form the phase-plate used to generate contrast and hence direct interpretation of
14 images can be challenging. A particular focus of the activity at Oxford is the coupling
15 of techniques to reconstruct the complex wavefunction at the exit-surface of the
16 sample from either a focal-series imaging geometry [7], or an illumination tilt-series
17
18
19
20
21
22
23
24
25 [8] using electron optically corrected image data.
26
27
28

29
30 Direct electron optical correction offers the advantage that it may be achieved
31 on line in a single image, with no requirement for post acquisition processing or
32 acquisition of extended image series. However, as already noted the correctors fitted
33 to both OJ1 and OJ2 instruments are only able to correct aberrations to third order,
34 with partial compensation of selected higher order terms for real recorded image data.
35
36
37
38
39
40
41 Thus, for aberration corrected instruments computational reconstruction is beneficial
42 as it provides a mechanism for compensation of for higher order aberrations and
43
44
45
46 enables the recovery of the complex specimen exit surface wavefunction.
47
48
49

50
51 When used in combination, direct aberration correction and exit wave
52 reconstruction provide additional advantages. For focal series datasets, the elimination
53 of tilt-induced coma relaxes the requirement for using parallel illumination and
54
55
56
57
58 enables the illumination to be converged onto the specimen area of interest. In this
59
60 mode, the current density at the sample may be maintained with a reduced source

1
2
3 emitter current and consequently lower energy spread in the illumination, providing
4 an improved information limit. For a tilt series dataset, the elimination of tilt induced
5 coma gives rise to less critical focus conditioning for any given tilt magnitude and
6 multiple tilt magnitudes are feasible without a large induced focus change. For either
7 data acquisition geometry, the reduced delocalisation in corrected images is
8 advantageous for quantitative interpretation. Finally, in aberration corrected
9 instruments the voltage centre and axial coma free axis are coincident and hence the
10 temporal coherence envelope is symmetric.
11
12
13
14
15
16
17
18
19
20
21
22
23
24

25 To illustrate the potential benefits of a combined direct / indirect approach to
26 aberration correction and compensation, Figure 2(a) shows the phase of the specimen
27 exit surface wavefunction of a Pt catalyst nanoparticle, viewed close to a $\langle 110 \rangle$
28 direction reconstructed from a focal series of aberration corrected images acquired
29 using the OJ1 instrument [9]. Despite the presence of a partially graphitic carbon
30 support, terraces and steps at the edge of the particle are visible and moreover, the
31 visibility, and spatial resolution of these features are improved significantly compared
32 to a conventional HRTEM image. The monatomic steps that are visible in Figure 2
33 are conventionally termed *A* or *B* type, with either $\{100\}$ or $\{111\}$ microfacet atomic
34 risers that have different catalytic properties. The peaks in the recovered phase can be
35 related to the number of Pt atoms in each atomic column and can thus be used to
36 obtain information about the local atomic arrangement on each surface in projection
37 (Figures 2(b) and (c)). Detailed analysis of these provides evidence that the outermost
38 atomic layers consist of irregular islands of atoms, in contrast to the atomic
39 arrangements that have been proposed on the basis of homoepitaxial growth
40 experiments on extended Pt surfaces.
41
42
43
44
45
46
47
48
49
50
51
52
53
54
55
56
57
58
59
60

1
2
3
4
5
6
7
8
9
10
11
12
13
14
15
16
17
18
19
20
21
22
23
24
25
26
27
28
29
30
31
32
33
34
35
36
37
38
39
40
41
42
43
44
45
46
47
48
49
50
51
52
53
54
55
56
57
58
59
60

Our next example demonstrates experimental verification of the resolution improvement possible using aberration corrected tilted illumination images. This requires a specimen with a real space lattice separation beyond the axial information limit and a gold foil oriented along a $\langle 123 \rangle$ direction satisfies this requirement. Figure 3 compares the phases and moduli of exit wavefunctions restored using both focal series and tilt defocus aberration corrected data sets. The only Fourier space detail present in the phase and modulus of the exit wavefunction (Figure 3 (c)) recovered from the focal series dataset relates to the $\{111\}$ planes, with a 0.235 nm lattice spacing. In contrast, the wavefunction recovered using tilted illumination data (Figure 3 (f)) contains information at the positions of the $\{331\}$, $\{420\}$ and $\{242\}$ lattice reflections, corresponding to real space distances of 0.093 nm, 0.091 nm and 0.083 nm .

Although the data presented in this section clearly demonstrates that a combination of direct aberration correction and exit wave reconstruction is advantageous and moreover, that the tilt azimuth acquisition geometry enables super-resolution, it is useful to examine the limiting factors in this approach. At large beam tilt magnitudes partial temporal coherence causes a loss of transfer at the centre of the tilted transfer function. For a beam tilt, $\tau_0 = \lambda \mathbf{k}_0$, beams at the same angle τ_0 with respect to the tilt axis are perfectly transferred and the temporal coherence envelope has no effect. However, for larger beam tilts the transfer falls away significantly inside this ring of perfect transfer (the achromatic circle). Reducing the tilt angle prevents this central transfer loss but reduces the resolution potential improvement. This reduction in transfer for tilted illumination can in principal be overcome either

1
2
3 by increasing the number of azimuthal angles or by including more than one tilt
4 magnitude in the restoration dataset. However, either of these approaches increases
5 the number of images required with consequent implications for experimental stability
6 required and for the overall radiation dose. The second limiting factor is given by the
7 variation in the experimentally measured axial aberration coefficients with
8 illumination tilt which can be estimated by taking the real part of the expansion of the
9 wave aberration function with respect to the complex aberration coefficients and
10 illumination tilt angle. Thirdly, in contrast to exit wavefunction reconstruction using
11 focal series data the individual images within a tilt series data set are not simply
12 different measurements of the same projected specimen potential. For tilted
13 illumination the specimen potential is projected along a slightly different direction
14 compared to the axial case and this introduces an additional phase shift. This can be
15 estimated using a simple geometric parallax model and choosing a maximum phase
16 variation for a resolvable distance, d as $\pm\pi/2$, the maximum parallax allowed between
17 the top and bottom specimen surfaces relative to the middle of the specimen is $d/4$.
18 For a beam tilt, τ_0 , this leads to a maximum specimen thickness of $d/(2\tau_0)$. This simple
19 geometric parallax argument is independent of the imaging conditions but has been
20 found to be more stringent than the tilt limit determined from a full dynamical
21 calculation.

22
23
24
25
26
27
28
29
30
31
32
33
34
35
36
37
38
39
40
41
42
43
44
45
46
47
48
49
50
51 These limits for exit wavefunction reconstruction using tilted illumination
52 images are summarised in Table 1. This clearly demonstrates that the aperture
53 synthesis approach to exit wavefunction reconstruction can be carried out using
54 datasets recorded at larger tilt magnitudes under aberration corrected imaging
55 conditions, giving rise to the possibility of resolution improvement substantially

1
2
3 beyond the axial information limit. However at extremely high resolution, parallax
4
5 considerations become increasingly significant leading to a new regime in which
6
7 sample thickness limits the resolution achievable.
8
9

10 11 12 13 **3. Aberration Corrected STEM Imaging**

14
15 The advantages of aberration-correction in a STEM geometry are that it provides
16
17 smaller illuminating probes together with higher beam currents as has been described
18
19 previously [10,11]. A sextupole corrector, identical to the one described earlier for
20
21 HRTEM imaging, is used to correct the pre-specimen optics operating in an
22
23 effectively inverted configuration. However, for STEM imaging it is not necessary to
24
25 correct for off-axial aberrations since the image is scanned and the scan coils can be
26
27 placed between the corrector and the objective lens such that the corrector is always
28
29 axially aligned relative to the illuminating beam. The relaxation of this constraint
30
31 allows the round 5th-order aberration (C_5) to be nulled by adjusting the transfer lenses
32
33 such that the negative C_5 combination aberration [6], generated by the deliberate mis-
34
35 projection of the corrector with respect to the objective lens, compensates for the
36
37 inherent C_5 arising from pre-field of the objective lens. The limiting aberration for
38
39 STEM is thus six-fold astigmatism, as is clearly demonstrated in the Ronchigram
40
41 shown in Figure 4. In the STEM geometry, alignment of the corrector is achieved
42
43 using an automated procedure developed by CEOS that relies on annular dark-field
44
45 (ADF) images of nanoparticles recorded at various, known illumination tilts through
46
47 the corrector and objective lens system. In practice we have found that 3rd-order
48
49 aberrations are stable over weeks of operation (as is also the case for alignment of the
50
51 lower corrector) and consequently day-to-day tuning of the lower order aberrations is
52
53 generally performed manually by direct observation of the Ronchigram.
54
55
56
57
58
59
60

1
2
3
4
5
6
7
8
9
10
11
12
13
14
15
16
17
18
19
20
21
22
23
24
25
26
27
28
29
30
31
32
33
34
35
36
37
38
39
40
41
42
43
44
45
46
47
48
49
50
51
52
53
54
55
56
57
58
59
60

In addition to the aberration corrector and associated coupling optics, a three condenser lens system completes the illumination optics of which two are the standard JEOL condenser lenses, with an additional third adaptor lens inserted before the corrector to ensure correct coupling. These three pre-corrector lenses allow independent adjustment of the source demagnification and beam convergence angle enabling beam currents of up to 2 nA and convergence angles of up to 32 mrad to be readily be achieved in the OJ2 instrument.

ADF imaging is the most widely used mode in the STEM geometry as it enables direct incoherent imaging of materials with a recorded intensity that depends strongly on atomic number [12]. This method was successfully applied by Cockayne and co-workers using the 2200FS (OJ1) instrument in an investigation of the distribution of rare earth dopant atoms in intergranular ceramic films [13]. These intergranular films play an important role in controlling the physical properties of many ceramic materials and doping with rare-earth metals has been shown to act as a sintering aid improving crack resistance. In order to explain observed differences in grain anisotropy in Si_3N_4 ceramics doped with different rare-earth elements, Cockayne and co-workers [13] used the 2200FS (OJ1) instrument to record aberration corrected ADF STEM images along different crystallographic directions for sample containing La and Lu (Figure 5). The aim of the study was to explain why La is more effective than Lu in elevating toughness. The Z-contrast nature of the ADF images allow the dopant atoms to be observed in the intergranular film, and preferential sites are seen for the dopants in the notionally amorphous volume. As can be seen in Fig. 5, data was recorded for the same system along two perpendicular directions, thereby allowing the three-dimensional position of the additive elements to be measured

1
2
3 quantitatively. Such quantitative measurements, quoted along with estimated errors,
4
5 had not achieved before in earlier studies on this system.
6
7
8
9

10
11 More recently, progress has been made in improving the quantification of
12
13 ADF STEM images. In addition to quantitatively measuring atom positions, there has
14
15 been progress in making quantitative use of image intensities by calibration of the
16
17 detector in terms of the fraction of the incident beam detected [14] and using
18
19 quantitative comparisons with simulations [15]. A crucial step in this approach is to
20
21 quantitatively map the efficiency of the detector as a function of detection position. In
22
23 both the OJ1 and OJ2 instruments the STEM detectors are located in the same optical
24
25 plane as the HRTEM imaging detectors and in order to collect a range of scattering
26
27 angles, as is required for STEM imaging, the post-specimen optics are adjusted to
28
29 diffraction mode. However, if the post-specimen optics are changed to imaging mode,
30
31 a magnified image of the STEM probe is formed in the image plane. In this latter
32
33 configuration, scanning the STEM probe with suitable adjustment of the
34
35 magnification enables the probe image can be scanned over the ADF detector
36
37 allowing its efficiency to be mapped. The OJ2 instrument is fitted with two ADF
38
39 detectors located before and after the omega energy filter. Operation of the pre-filter
40
41 detector is more straightforward since high-angle scattering does not need to pass
42
43 through the energy-filter, obviating the need for accurate filter alignment. An
44
45 efficiency map of this detector is shown in Figure 6 and as is the case for most ADF
46
47 detectors, it is evident that the response is non-uniform which must be considered
48
49 when extracting quantitative information from ADF images.
50
51
52
53
54
55
56
57
58
59
60

1
2
3
4 For quantitative ADF STEM imaging, calibration of the digitized intensity
5 values in terms of the incident beam is necessary. Typical fractions of the incident
6 beam scattered onto the ADF detector are usually around 10%. On the OJ2
7 instruments, a routine procedure for quantitative ADF STEM imaging has been
8 developed. In this method the condenser optics are adjusted such that the incident
9 beam current is reduced to *ca.* 10% of the nominal value used for imaging and this
10 reduced beam current is used to measure the detector map. If the fractional reduction
11 in current is accurately measured using a Faraday cup, the signal measured in any
12 subsequent experiment will be calibrated in terms of fraction of the incident beam
13 current. This approach is valid as long as the detector amplifier contrast (gain) and
14 brightness (offset) are not altered after the initial calibration because experiments
15 have shown that the detector response is linear with respect to beam current [16].
16 Under these conditions, images can be recorded that are calibrated such that the
17 intensity of the image is expressed as the fraction of the primary beam electrons that
18 are scattered to the ADF detector. Figure 7 shows such an image of a core-shell
19 catalyst nanoparticle comprising a Pd core and Pt shell. The aim of the synthesis is to
20 generate a monolayer of Pt conformally covering the Pd core. There is clear evidence
21 for the Pt shell in the image, but the relatively straight boundaries to the brighter Pt
22 regions suggest that the Pt shell has coverage only on particular facets. The high
23 signal-to-noise ratio available in aberration-corrected STEM allows the terminating
24 atomic columns and several single atoms decorating the surrounding carbon support,
25 to be readily observed. Recording such calibrated data will now allow a direct
26 comparison with simulation allowing more detailed quantitative analysis
27
28
29
30
31
32
33
34
35
36
37
38
39
40
41
42
43
44
45
46
47
48
49
50
51
52
53
54
55
56
57
58
59
60

1
2
3 For quantitative comparison between experiments and simulations, a
4 parameter that can be particularly challenging to quantify is the effective source size
5 measured at the sample [17]. By the principle of reciprocity, this parameter plays the
6 same role as the modulation transfer function (MTF) of the detector in HRTEM
7 imaging [18]. However, as already described, in both the Oxford-JEOL instruments
8 the post-specimen optics allow a aberration free image of the STEM probe to be
9 recorded and this may provide a method for the measurement of STEM imaging
10 parameters more accurately. We also note that accurate imaging of the STEM probe
11 can also be a powerful diagnostic tool for the analysis of instabilities where it
12 provides a sample-independent measurement.
13
14
15
16
17
18
19
20
21
22
23
24
25
26
27
28

29 **4. Confocal Imaging**

30
31 The ability to form an aberration free image of a STEM probe, as outlined in the
32 previous section, enables confocal imaging using trajectories analogous to those used
33 in confocal light microscopy. Scanning confocal electron microscopy (SCEM) was
34 first demonstrated in uncorrected TEM by Frigo and coworkers [19] in an application
35 to the specific problem of imaging thick samples. One of the key advantages of the
36 confocal scanning optical microscope (CSOM), however, is the retrieval of three-
37 dimensional imaging through the process of optical sectioning.
38
39
40
41
42
43
44
45
46
47
48
49
50

51 In general the depth of focus, Δz , for an optical system with a wavelength, λ ,
52 is given by [20]
53

$$54 \Delta z \approx \frac{\lambda}{\sin^2 \alpha} \quad (1)$$

55
56
57
58
59
60

1
2
3 where α is the semi-angle subtended by the focusing lens at the sample. In the case of
4
5 light optics this value approaches the wavelength of the light. However, in an
6
7 uncorrected electron microscope α typically takes values close to 0.01 and hence Δz
8
9 has values of tens of nanometers, which is larger than the typical thickness of a TEM
10
11 sample. Aberration correction, however, has a dramatic effect on the depth of focus as
12
13 an increase of a factor of three in α reduces the depth of focus by a factor of nine,
14
15 leading to values of just a few nanometers, substantially less than typical sample
16
17 thicknesses.
18
19
20
21
22
23
24

25 Using this reduced depth of focus to retrieve 3D information in STEM has
26
27 been demonstrated previously [21, 22]. In a non-confocal geometry, however, this
28
29 approach can only be used for high-resolution imaging as the 3D transfer function for
30
31 incoherent STEM imaging shows a missing cone which results in significant
32
33 elongation in 3D images of laterally extended objects [23]. One of the motivations for
34
35 the development of SCEM is the removal of this out-of-focus blurring in the image.
36
37 Figure 8 schematically shows that in the confocal configuration, a small collector
38
39 aperture placed in the detector plane rejects scattering away from the confocal point
40
41 leading to improve depth resolution and selectivity.
42
43
44
45
46
47
48

49 Various authors [24-26] have considered the contrast observed in a confocal
50
51 geometry and in particular Cosgriff et al. [24] have shown that first-order phase
52
53 contrast is not transferred in a confocal configuration. Therefore, the conventional
54
55 “bright-field” imaging mode in the SCEM geometry will have limited application.
56
57 However, a more promising imaging mode is available in the 2200MCO instrument
58
59 that makes use of both aberration correctors together with the in-column energy-filter,
60

1
2
3
4
5
6
7
8
9
10
11
12
13
14
15
16
17
18
19
20
21
22
23
24
25
26
27
28
29
30
31
32
33
34
35
36
37
38
39
40
41
42
43
44
45
46
47
48
49
50
51
52
53
54
55
56
57
58
59
60

whereby it is possible to use the instrument as an energy-filtered scanning confocal electron microscope (EFSCEM). Importantly, it has been shown [25,27] that this mode does not suffer from a missing cone in the transfer function, and therefore extended objects can be imaged with maximum depth resolution.

The instrumental alignment for confocal experiments is challenging. A method for simultaneously tuning the optical elements required to form an aberration-corrected focused probe illuminating the sample and aberration-corrected post-specimen optics subsequently focusing that probe to the detector plane has been previously described [28]. This involves using the electron Ronchigram to achieve tuned STEM optics, then switching the post-column optics to imaging mode such that a probe image is observed on a CCD camera. Making the assumption that the STEM probe is tuned, the post-specimen optics can be adjusted such that no aberrations are observed in the probe image. Figure 9 shows such a probe where some residual three-fold astigmatism can be seen.

A particular difficulty with EFSCEM, however, is that a change in energy of the electrons of interest by inelastic scattering in the sample, combined with the chromatic aberration of the post-sample optics, defocuses the post-specimen optics. A method has been devised [29] in which the incident beam energy is changed by adjusting the high tension supply such that the confocal configuration is regained for electrons that suffer a specific energy loss in the sample (Figure 10), where it is evident that scattering is only brought to focus at the specific energy loss of interest.

Making use of such a configuration, Figure 11 shows the improvement in depth resolution that results from using the EFSCEM mode [29]. A purpose designed

1
2
3 piezo-driven stage-scanning system [30] was used to acquire two-dimensional lateral
4 (x - y) scans, or alternatively to slice in depth by scanning along one lateral direction
5
6 (x - y) scans, or alternatively to slice in depth by scanning along one lateral direction
7
8 and the depth direction to form an (x - z) scan. A carbon film decorated with Au
9
10 nanoparticles was used as a test sample and the microscope was adjusted to the
11
12 confocal mode for the carbon K-edge scattering. Figures 11(a) and 11(d) compare
13
14 EFSCEM lateral x - y scans acquired with the sample positioned at the confocal height
15
16 with and without a collector aperture present. Without a collector aperture, all the
17
18 scattered intensity collected by the post-specimen lens contributes to the image, and
19
20 this mode is therefore similar to energy-filtered STEM (EFSTEM) imaging and
21
22 cannot be regarded as being a confocal. Figures 11(b) and 11(e) compare scans in the
23
24 x - z plane at positions corresponding to $y=0$ nm in Figs. 11(a) and (d) respectively.
25
26
27
28

29
30 The FWHMs of the intensity profiles L1 and L2 collected in EFSTEM modes
31
32 (Fig. 11c) are more than 1 μm . In the EFSTEM mode, the out-of-focus scattered
33
34 electrons are collected so this geometry cannot distinguish the different film
35
36 thicknesses as expected. In the EFSCEM mode, rejection of scattering away from the
37
38 confocal plane occurs and the data shows a FWHM in the depth direction of
39
40 84 ± 21 nm and 42 ± 21 nm at points 1 and 2, respectively (Fig. 11(f)). Thus direct
41
42 imaging of the change in thickness of the carbon film can be observed using
43
44 EFSCEM, and it can be seen that there are significant variations in the height of the
45
46 carbon film between points 1 and 2. Work is currently underway to explore the range
47
48 of application of this new technique.
49
50
51
52
53
54
55
56

57 **5. Conclusions**

58
59
60

1
2
3
4 In this paper we have reviewed the ways in which the aberration-corrected electron
5
6 microscopes developed in partnership between Oxford and JEOL have been used
7
8 since 2003. We firstly describe the advantages and ultimate limitations of combining
9
10 aberration corrected TEM imaging with exit wavefunction reconstruction with
11
12 particular reference to a tilt azimuth dataset geometry. Subsequently we review the
13
14 use of ADF STEM imaging in studies of ceramic grain boundary interfaces carried
15
16 out by David Cockayne's group and also describe recent progress in quantification of
17
18 the ADF signal. Differences in the optimum way of operating the correctors for
19
20 HRTEM and STEM have been discussed. Finally, the development of a new confocal
21
22 mode of microscopy has been described, making use of the unusual optical
23
24 configuration of the instrument.
25
26
27
28
29
30
31
32

33 Acknowledgements

34
35 The authors would like to acknowledge financial support from the Leverhulme Trust (F/08 749/B) and
36
37 the EPSRC (EP/F048009/1) and Intel Ireland. Technical assistance from JEOL Ltd and JEOL (UK) Ltd
38
39 is also acknowledged.
40
41
42
43
44
45
46
47
48
49
50
51
52
53
54
55
56
57
58
59
60

References

- [1] J. L. Hutchison, J. M. Titchmarsh, D. J. H. C. Cockayne, R. C. Doole, C. J. D. Hetherington, A. I. Kirkland, H. Sawada, *Ultramicroscopy*, **103**, 7 (2005).
- [2] A. I. Kirkland, J. M. Titchmarsh, J. L. Hutchison, D. J. H. Cockayne, C. J. D. Hetherington, R. C. Doole, H. Sawada, M. Haider, P. Hartel, *JEOL News*, **39(1)**, 2 (2004).
- [3] K. Tsuno, T. Kaneyama, T. Honda, K. Tsuda, M. Terauchi, M. Tanaka, *J. Electron Microscopy* **46**, 357 (1997).
- [4] H. Rose, *Optik* **85**, 19 (1990).
- [5] M. Haider, H. Rose, S. Uhlemann, E. Schwan, B. Kabius and K. Urban, *Ultramicroscopy* **75**, 53 (1998).
- [6] P. Hartel, H. Müller, S. Uhlemann, and M. Haider, *Proceedings of EMC 2004, Antwerp*, 41 (2004).
- [7] A. I. Kirkland, R. R. Meyer, *Microscopy and Microanalysis* **10**, 1 (2004).
- [8] S. Haigh, H. Sawada, A. I. Kirkland, *Phil. Trans. Proc. Roy. Soc A* **367**, 3755 (2009).
- [9] L. Cervera Gontard, L.-Y. Chang, C. J. D. Hetherington, A. I. Kirkland, D. Ozkaya, and R. E. Dunin-Borkowski, *Angew. Chem.* **46**, 3683 (2007).
- [10] N. Dellby, O. L. Krivanek, P. D. Nellist, P. E. Batson, and A. R. Lupini, *Journal of Electron Microscopy* **50**, 177 (2001).
- [11] M. Haider, S. Uhlemann, and J. Zach, *Ultramicroscopy* **81**, 163 (2000).
- [12] P. D. Nellist, S. J. Pennycook, *Adv. Imaging & Electron Phys.* **113**, 148 (2000).
- [13] G. B. Winkelman, C. Dwyer, T. S. Hudson, D. Nguyen-Manh, M. Doblinger, R. L. Satet, M. J. Hoffmann and D. J. H. Cockayne, *Appl. Phys. Lett.* **87**, 061911 (2005).
- [14] J. M. LeBeau, S. Stemmer, *Ultramicroscopy* **108**, 1653 (2008).
- [15] J. M. LeBeau, S. D. Findlay, L. J. Allen, and S. Stemmer, *Phys. Rev. Lett.* **100**, 4 (2008).
- [16] H. E. P. D. Nellist, S. Lozano-Perez and D. Ozkaya in *Proc. EMAG2009*, IOP Publishing (2010).
- [17] P. D. Nellist, Chapter 2 (pp 65-132) in *Science of Microscopy*, Ed. P. W. Hawkes, J. C. H. Spence, Springer, New York (2008).
- [18] R. R. Meyer, A. I. Kirkland, *Ultramicroscopy* **75**, 23 (1998).
- [19] S. P. Frigo, Z. H. Levine, N. J. Zaluzec, *Appl. Phys. Lett.* **81**, 2112 (2002).
- [20] M. Born, E. Wolf, *Principles of Optics*. Pergamon Press, Oxford (1980).
- [21] K. Van Benthem, A. R. Lupini, M. Kim, H. S. Baik, S. Doh, J.-H. Lee, M. P. Oxley, S. D. Findlay, L. J. Allen, J. T. Luck, and S. J. Pennycook, *Applied Physics Letters* **87**, 034104 (2005).
- [22] Borisevich, A.Y., Lupini, A.R., and Pennycook, S.J., *Proc. Natl. Acad. Sci.* **103** 3044 (2006).
- [23] G. Behan, E. C. Cosgriff, A. I. Kirkland, and P. D. Nellist, *Phil. Trans. R. Soc. Lond., A* **367**, 3825 (2009).

- 1
2
3 [24] E. C. Cosgriff, A. J. D'Alfonso, L. J. Allen, S. D. Findlay, A. I. Kirkland, and
4 P. D. Nellist, *Ultramicroscopy* **108**, 1558 (2008).
5
6 [25] A. J. D'Alfonso, E. C. Cosgriff, S. D. Findlay, G. Behan, A. I. Kirkland, P. D.
7 Nellist, and L. J. Allen, *Ultramicroscopy* **108**, 1567 (2008).
8
9 [26] J. J. Einspahr, P. M. Voyles, *Ultramicroscopy*, **106**, 1041 (2006).
10
11 [27] H. L. L. Xin, D. A. Muller, *J. Electron Microsc.*, **58**, 157 (2009).
12
13 [28] P. D. Nellist, G. Behan, A. I. Kirkland, and C. J. D. Hetherington, *Applied*
14 *Physics Letters* **89**, 124105 (2006).
15
16 [29] P. Wang, G. Behan, M. Takeguchi, A. Hashimoto, K. Mitsuishi, M. Shimojo,
17 A. I. Kirkland and P. D. Nellist, *Physical Review Letters* **104**, 200801 (2010).
18
19 [30] M. Takeguchi, A. Hashimoto, M. Shimojo, K. Mitsuishi and K. Furuya J.
20 *Electron Microsc.*, **57**, 123 (2008).
21
22
23
24
25
26
27
28
29
30
31
32
33
34
35
36
37
38
39
40
41
42
43
44
45
46
47
48
49
50
51
52
53
54
55
56
57
58
59
60

Table 1. Tilt limits determined for an object thickness of 2 nm at 200 kV assuming third order aberration correction and a focal spread = 4 nm.

Limiting Factor	Maximum Tilt Magnitude /mrad	Resolution Limit /nm
Incoherent Aberrations	19	0.0629
Coherent Aberrations	25	0.0547
Geometric Parallax	18	0.0645

For Peer Review Only

Figure captions

Figure 1. The Oxford-JEOL aberration corrected microscopes (a) JEM 2200FS installed in 2003, (b) JEM 2200 MCO installed in 2006.

Figure 2. (a) Restored phase of a 6-nm Pt particle obtained by applying spherical aberration correction and through-focus exit wavefunction restoration to a defocus series of 20 images acquired on the OJ1 instrument at 200 kV with $C_3=30 \mu\text{m}$ (b) Best fitting simulated phase from multislice calculations of the exit plane wavefunction for various terrace structures. The best match is taken to be the one in which the ratio of simulated phase shifts between individual atomic columns in the terraces best matches the experimentally measured ratios at equivalent positions. The magnitudes of the simulated phase shifts, both on the terraces and in the center of the particle, are higher in the simulations than in the experimental data. This difference may provide insight into the poorly understood discrepancy between the contrast of simulated and experimental conventional HRTEM images, known as the Stobbs factor. (c) Three dimensional atomic model used to calculate the best-fitting phase in part (b). The large white arrow indicates the direction of the electron beam. The insets in (a) and (b) show the crystallographic details of the particle. In parts (b) and (c) 1–4 correspond to the same features on the surface of the particle. The notation Pt(S)- $n(x,y,z)K(u,v,w)$ refers to the microfacets for which n is the number of atoms in the terrace, (x,y,z) is the Miller index of the terrace, and (u,v,w) is the Miller index of the step.

Figure 3. Exit wavefunctions for a gold foil oriented along the $\langle 123 \rangle$ direction. (a), (b) (c) phase, modulus and Fourier transform of the exit wavefunction restored using a

1
2
3
4 16 image focal series with a focal step of 7 nm. (d), (e), (f) phase, modulus and
5
6 Fourier transform of the exit wavefunction of the same specimen area restored from a
7
8 27 image tilt-defocus data set with a maximum tilt magnitude of 18.4 mrad. The axial
9
10 10% information limit of 0.1 nm is indicated on both transforms for reference, and the
11
12 contrast in the transforms has been inverted but not otherwise scaled to improve
13
14 clarity.
15
16
17
18
19

20 Figure 4. A Ronchigram demonstrating the accuracy of aberration correction in the
21
22 STEM mode. The radius of the overlaid circle is 40 mrad. The 12-fold rotational
23
24 symmetry expected when the aberrations are dominated by six-fold astigmatism is
25
26 apparent.
27
28
29
30

31 Figure 5. Experimental HAADF-STEM images of {100} crystal-intergranular film
32
33 interfaces in rare-earth-containing Si_3N_4 . (a, b) La-containing Si_3N_4 viewed parallel to
34
35 [001] and [100], respectively. (c, d) Lu-containing Si_3N_4 viewed parallel to [001] and
36
37 [100], respectively. Reproduced from Ref. [14] with permission of the American
38
39 Institute of Physics.
40
41
42
43
44
45

46 Figure 6. The ADF detector efficiency as a function of probe position across the
47
48 detector surface, scaled to mean value across detector. Variations in efficiency are
49
50 seen across the detector surface, in particular at low angles.
51
52
53
54

55 Figure 7. An ADF STEM image of a Pd core/Pt shell nanoparticle with an intensity
56
57 scale calibrated as a fraction of the incident electron intensity. The detector inner
58
59 radius was 90 mrad.
60

1
2
3
4
5
6 Figure 8. Schematic diagram of the confocal trajectories for SCEM which shows that
7
8 the beams scattered away from the confocal point, a, are rejected by the collector
9
10 aperture.
11

12
13
14
15 Figure 9. The image recorded in the detector plane when the microscope is aligned
16
17 for confocal operation with no specimen present. In this mode, the post-specimen
18
19 optics are forming an image of the STEM probe. The probe current was measured to
20
21 be 20 pA.
22
23

24
25
26
27 Figure 10. An image of the intensity in the energy dispersion plane with the
28
29 microscope in a confocal configuration for a desired energy-loss of ~ 100 eV
30
31 corresponding to Si L-edge. A sample of Si is present and energy-loss features such
32
33 as plasmon-loss peaks may be seen. The beam can be seen to be coming to a focus,
34
35 indicating a confocal condition at the energy-loss of interest.
36
37

38
39
40
41 Figure 11. EFSCEM x - y scans acquired from a carbon film positioned at the confocal
42
43 point (a) without a collector aperture (EFSTEM equivalent) and (d) with a collector
44
45 aperture corresponding to a diameter of 0.34 nm. (b) and (e) EFSCEM x - z scans along
46
47 $y=0$ nm in (a) and (d), respectively. (c) and (f) line profiles along the dotted lines L1 (-
48
49 --) and L2 (---) shown in (b) and (e). (Reproduced from Ref [29] with permission of
50
51 the American Physical Society).
52
53
54
55
56
57
58
59
60

Figure 1



(a)



(b)

Figure 2

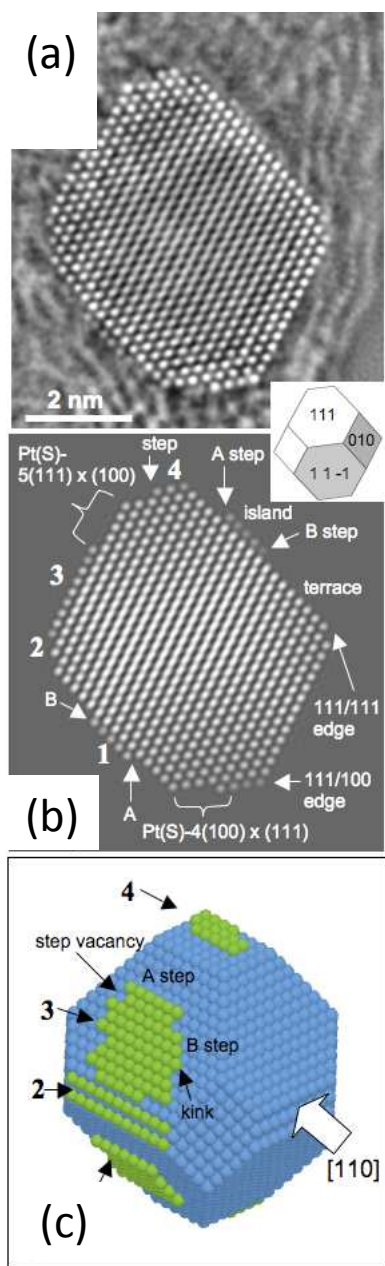


Figure 3

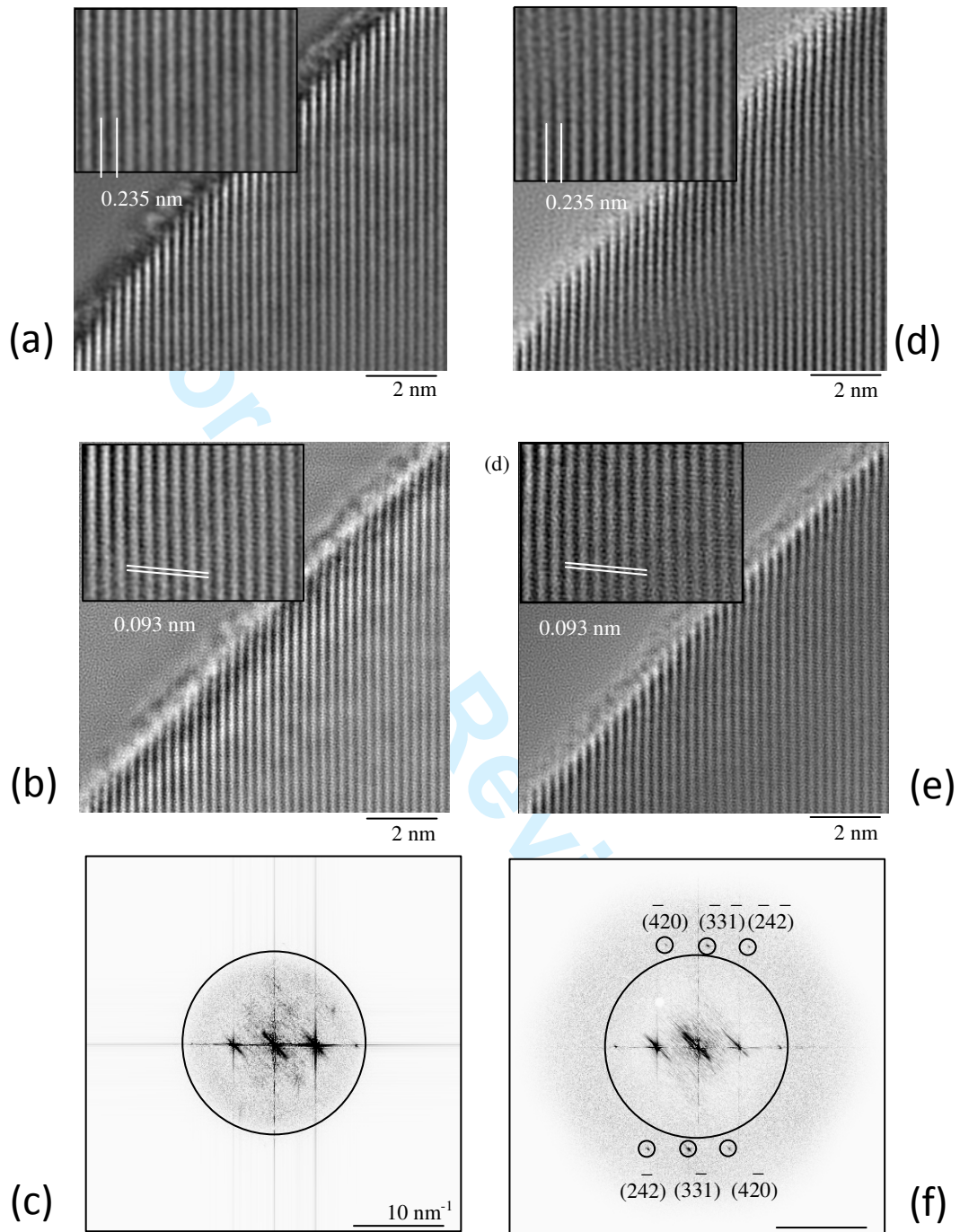


Figure 4

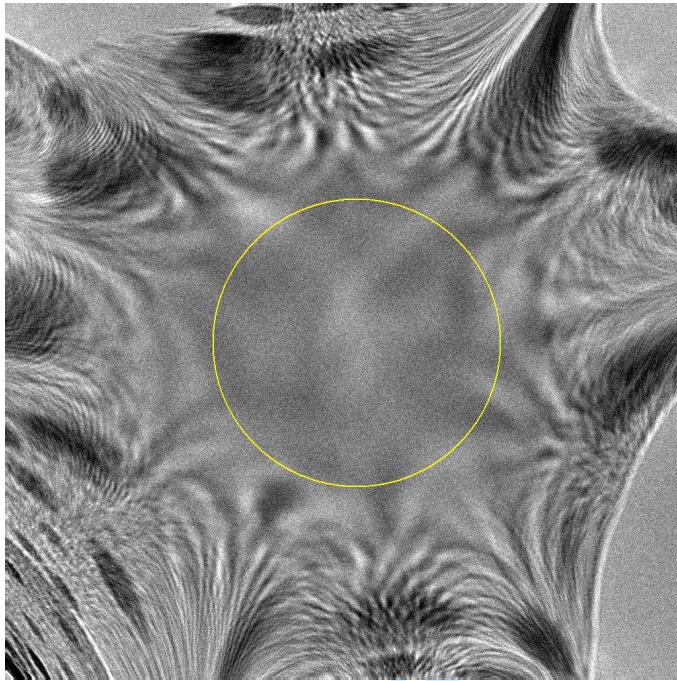


Figure 5

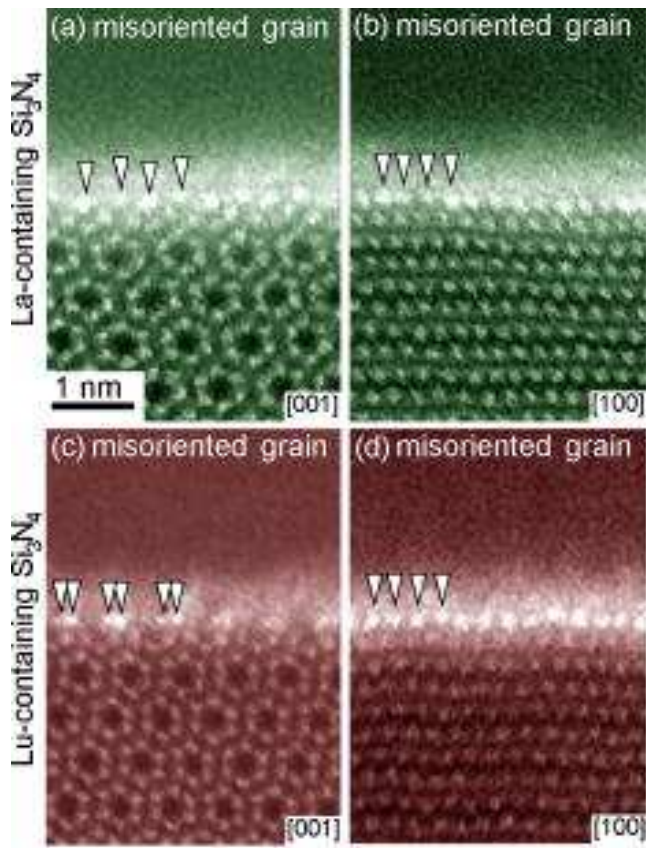
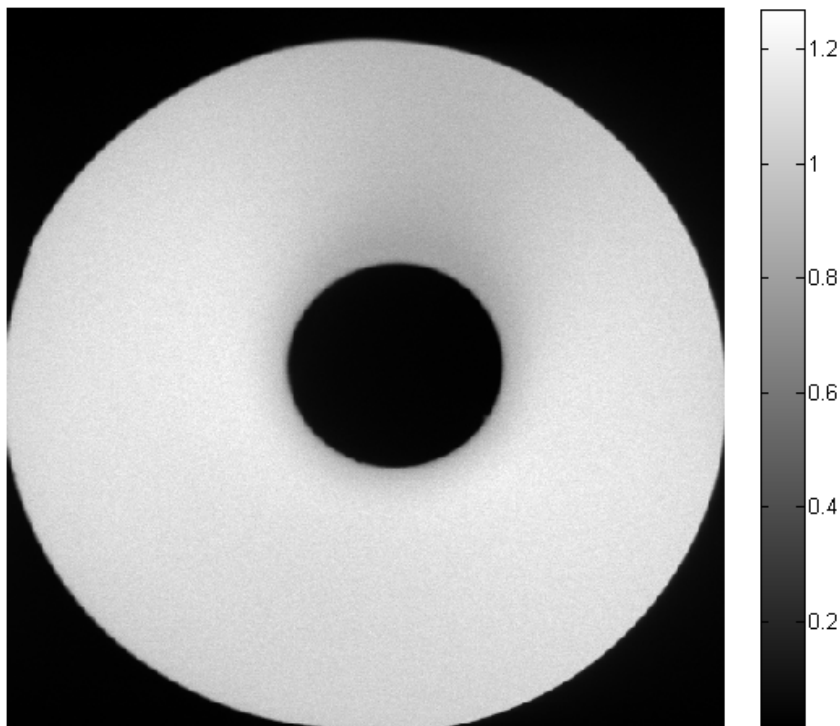


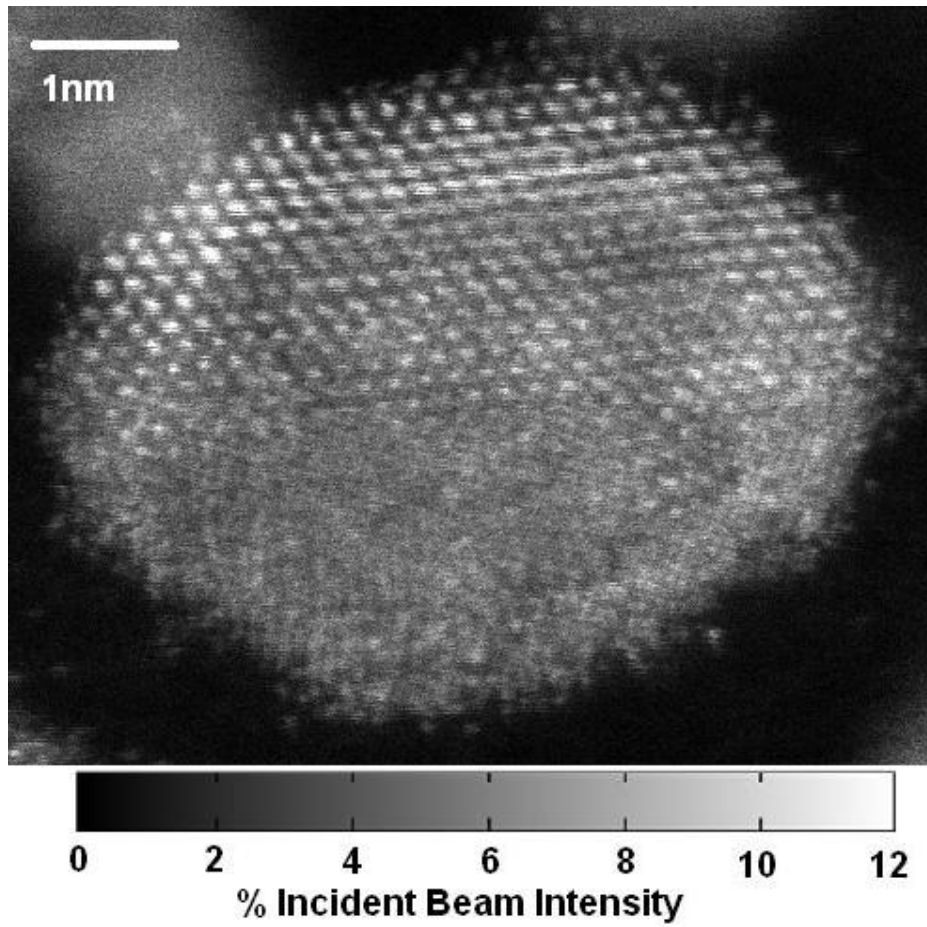
Figure 6



Review Only

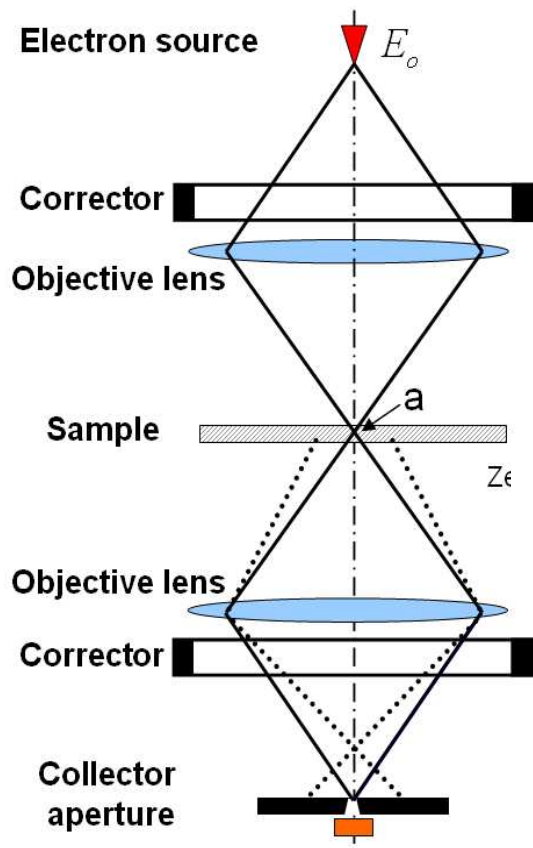
1
2
3
4
5
6
7
8
9
10
11
12
13
14
15
16
17
18
19
20
21
22
23
24
25
26
27
28
29
30
31
32
33
34
35
36
37
38
39
40
41
42
43
44
45
46
47
48
49
50
51
52
53
54
55
56
57
58
59
60

Figure 7



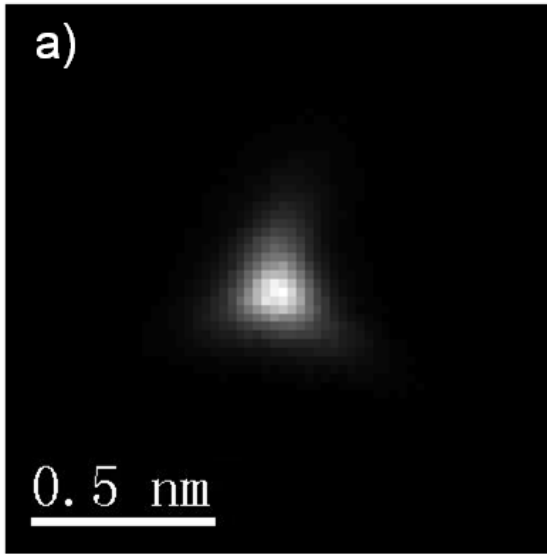
view Only

Figure 8



Review Only

Figure 9



Peer Review Only

Figure 10

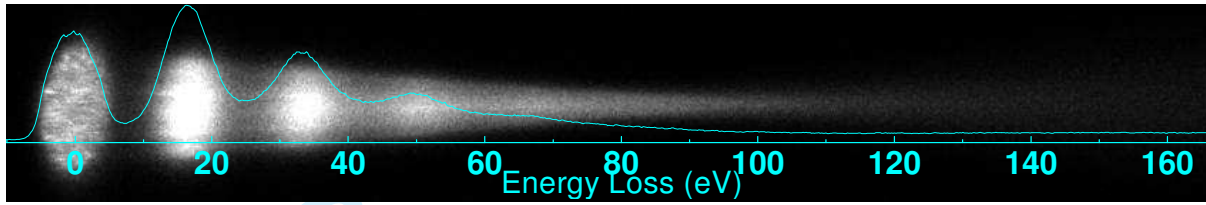


Figure 11

